Approximate model for analyzing band structures of single-ring hollow-core anti-resonant fibers

RON FATOBENE ANDO,[1,*] ALEXANDER HARTUNG,[1] BUMJOON JANG,[1] AND MARKUS A. SCHMIDT[1,2,3]

[1]*Leibniz Institute of Photonic Technology, Albert-Einstein-Str. 9, 07745 Jena, Germany*
[2]*Abbe Center of Photonics, Friedrich-Schiller-Universität Jena, Max-Wien-Platz 1, 07743 Jena, Germany*
[3]*Otto Schott Institute of Materials Research, Fraunhoferstr. 6, 07743 Jena, Germany*
[*]*ron.fatobene@leibniz-ipht.de*

Abstract: Precise knowledge of modal behavior is of essential importance for understanding light guidance, particularly in hollow-core fibers. Here we present a semi-analytical model that allows determination of bands formed in revolver-type anti-resonant hollow-core fibers. The approach is independent of the actual arrangement of the anti-resonant elements, does not enforce artificial lattice arrangements and allows determination of the effective indices of modes of preselected order. The simulations show two classes of modes: (i) low-order modes exhibiting effective indices with moderate slopes and (ii) a high number of high-order modes with very strong effective index dispersion, forming a quasi-continuum of modes. It is shown that the mode density scales with the square of the normalized frequency, being to some extent similar to the behavior of multimode fibers.

1. Introduction

Hollow core fibers received significant attention during recent times due to their extraordinary potential for a multitude of applications such as light generation and delivery in the UV [1–5] and mid-IR [6–11], spectroscopy [12–17], micromachining [18, 19], surgery [20] and low-latency data transmission [21, 22]. In particular, hollow-core anti-resonant fibers (HC-ARFs), consisting of a small number of anti-resonant elements (AREs) arranged around a hollow core, represent a promising alternative to existing fiber geometries due to their simplistic design compared to, e.g., Kagome or photonic band gap (PBG) fibers [6, 23, 24]. In contrast to the latter fiber type, light guidance in HC-ARFs is mediated by a combination of anti-resonant reflection at the air-silica interfaces and inhibited coupling [25–27] and does not demand a periodic microstructured cladding compared to PBG fibers. Within a first-order approximation, low-loss light guidance in HC-ARFs is associated with the close-to-unity reflectivity of a ray incident on the glass strand at nearly grazing incidence [28, 29].

A particularly important branch of HC-ARFs is the nodeless negative-curvature design (Fig. 1(a)), comprising mutually non-touching tubular AREs which are connected to the fiber jacket at a single location, resulting in reduced bend loss [30]. The negative-curvature core shape and the lack of nodes strongly reduce the number of modes the core mode could potentially couple to and thus, decrease the confinement loss [31, 32]. This loss reduction strategy is typically implemented on the basis of arranging a small number of tubular AREs around a central hollow core by attaching them at constant azimuthal distances to the inner wall of a jacket capillary. These fibers are referred to as revolver-type fibers, node-less HC-ARFs or single-ring PCFs and reveal enormous potential for the applications mentioned above. Additional features (e.g., nano-bridges or nested tubes) can also be included into the AREs in order to further reduce the confinement losses to telecommunication levels [4, 33–35], where an optimized thickness
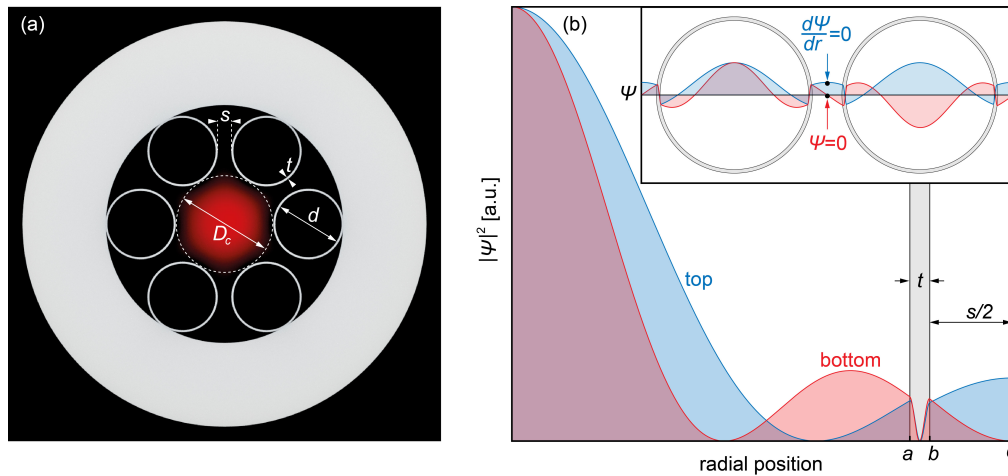
Fig. 1. (a) Illustration of the cross section of a single-ring anti-resonant hollow-core fiber (i.e., revolver-type hollow-core fiber). The geometric parameters shown in the sketch are explained in the main text. A typical, numerically calculated intensity distribution of the fundamental core mode is shown (red). (b) Examples of intensity distributions of the top and bottom band edge mode using our model (grey background: ARE strand). The inset shows two anti-resonant elements and the scalar field distributions of top and bottom band edge modes with the corresponding boundary condition highlighted by the two black dots.

of the air regions can also decrease losses [36]. Light guidance in HC-ARFs can be described as a combination of (i) anti-resonant reflection [26] and (ii) inhibited coupling between core and ARE modes [37]. An analysis of the guided modes is typically addressed by full-vectorial finite-element (FE) simulations. However, the large diameters of core and AREs allow for (circular and planar) approximations that enable predicting propagation constants and modal attenuation very well [28, 29, 38–41]. Since anti-resonant reflection is necessary but not sufficient for low-loss guidance of light in HC-ARFs, coupling of energy from the central core to the ARE modes needs to be avoided (referred to as inhibited coupling), which is usually achieved by an optimized ratio between core and ARE diameters.

To reveal the physics of light guidance in HC-ARFs, understanding the formation of bands mediated by the modes of the microstructured cladding is the essential key and was of great help to unlock the basic principles of light guidance in, e.g., band gap fibers [42] and planar photonic crystal structures [43, 44]. Considering infinitely extended lattices of defined symmetry (e.g., hexagonal lattice in case of PBG fibers) has been successfully employed to calculate the density of states (DOS) in microstructured claddings [45]. In contrast to PBG fibers, revolver-type HC-ARFs generally include a single ring of AREs which are circularly arranged at constant azimuthal distances.

Here, we present a semi-analytical model that allows calculating the edges of bands formed by the coupling of the ARE-modes in revolver-type HC-ARFs. The approach is independent of the actual arrangement of the AREs, does not enforce artificial lattice geometries to the single ARE and allows determining the propagation constants of cladding modes of preselected order. The effective indices obtained from the simulations show that (i) low-order modes are close to the dispersion of the central core mode and (ii) there exist a high number of higher-order, strongly-dispersive modes, forming a quasi-continuum of modes. Additionally, an analysis of the modes at cut-off shows that mode density scales with the square of the normalized frequency.

2. Fiber geometry and method

2.1. Fiber geometry

The geometry of the revolver-type HC-ARF considered here consists of N non-touching tubular AREs (inner diameter d, wall thickness t, gap width s) attached to the interior of a jacket-tube (Fig. 1(a)). Here we define three important parameters $a = d/2$, $b = a + t$ and $c = b + s/2$ along the radial axis of one ARE (Fig. 1(b)) which are required for the subsequent considerations. The core diameter D_c is determined by the size and number of AREs, given by [41]

$$D_c = 2\frac{c - b\sin\pi/N}{\sin\pi/N} \tag{1}$$

2.2. Proposed model

The mathematical model which we would like to introduce here was originally developed within the scope of all-solid PBG fibers by Birks et al [46]. The basic idea relies on determining the effective indices n_{eff} of top and bottom band edge modes via analyzing the supermodes of two identical adjacent cylindrical waveguides (field distributions: ψ). Due to the symmetry of this geometry these modes are obtained by applying boundary conditions exactly in the middle between the two waveguides: $d\psi/dr|_{r=c} = 0$ and $\psi(r = c) = 0$ (see Fig. 1(b)). The resulting band edge modes resemble bonding and anti-bonding states well-known from the hybridization of wave functions in molecular physics (e.g. H_2 molecule). The effective indices of other possibly formed supermodes are located inside the range defined by these two edges, simplifying the analysis to the calculation of only two modes in order to distinguish domains of zero and non-zero density of cladding states. Please note, that a generalized model for an arbitrary number of layers using a transfer matrix approach was already introduced earlier [47]. However, the particular symmetrical case of three layers relevant here (air-silica-air) enables a comparably simple expression of the dispersion equation of the band edge modes without using matrix equations.

It is important to note that the discussed model is in fact a one-dimensional nearest-neighbor approach. This particular fact makes this model highly appropriate to analyze the cladding modes of revolver-type HC-ARFs in comparison to numerical calculations of the photonic density of states which demands to artificially impose infinite periodic symmetries to the structure. Within the scope of the single ring anti-resonant fiber geometry investigated here (Fig. 1(a)), the interaction of adjacent AREs can be assumed to be that of an infinite azimuthal chain of AREs with only neighboring elements interacting (nearest-neighbor approximation) with no energy flux along this direction. The energy flow along the radial direction can be neglected here since simulations of a single anti-resonant element show that the imaginary part of the effective index is about 10^5 to 10^6 times smaller than that of the real part for realistic geometry parameters (ARE diameter about 20 µm). Since our model relies on scalar wave functions (i.e., the weak-guidance approximation), we verify its applicability by comparing the effective indices of the modes of a single ARE obtained from FE simulations and from the scalar wave approximation (see Appendix, Fig. 7). This direct comparison shows a negligible difference between both approaches across almost the entire relevant spectral bandwidth, justifying the scalar wave approximation. Please note, that the scalar wave approximation has been successfully applied to situations of significantly higher refractive index contrast (chalcogenide/silica PBG fibers [48]), whereas it can principally be extended to account for the vectorial nature of Maxwell's equations [49]. The effective indices of the edge modes are obtained by solving the dispersion equation of the three-layer system using the particular boundary conditions (see Appendix).

3. Results and discussion

3.1. Investigated geometry

The geometric parameters of the revolver-type HC-ARF considered here are $N = 6$, $d = 20\,\mu m$, $t = 500\,nm$ and $s = 4.16\,\mu m$, yielding a core size of $D_c = 29.33\,\mu m$ using Eq. (1), corresponding to typically implemented revolver-type HC-ARFs. It is important to note that the resulting ratio $d/D_c = 0.682$ yields a phase-matching between the first higher-order core mode and the fundamental ARE mode, leading to large modal differential loss as proposed by [28, 50]. For the sake of simplicity the material dispersion of silica and air have been neglected here, yielding constant refractive indices (refractive index glass $n_g = 1.45$, refractive index air $n_a = 1$). The use of dispersion-less material parameters allows a scaling-invariant representation of the results using the planar V-parameter given by $V = k_0 t (n_g^2 - n_a^2)^{1/2}$, which linearizes the spectral dependence of the modes and directly shows the spectral positions of the resonances at multiple integers of π.

3.2. ARE modes inside the fundamental transmission band

In the following we show the spectral distributions of the normalized effective mode index $(n_{\text{eff}} - n_a)V^2$ of the various relevant modes, whereas we refer to the resulting plots as band maps. Here, the scaling factor V^2 removes the strong waveguide dispersion which is usually present in such plots in order to improve visibility of the band maps. The particular choice of the scaling factor is motivated by the λ_0^{-2}-scaling known from the Marcatili-Schmeltzer model [51] and leads to constant values of $(n_{\text{eff}} - n_a)V^2$ of a particular mode at the points of anti-resonance ($V = \pi/2$, $3/2\pi, 5/2\pi,...$) in the absence of material dispersion.

Special care has to be taken regarding the assignment of mode labels. The labeling of LP modes corresponds to a pre-chosen azimuthal mode order l and the incremental solution counter m. Since reported studies on antiresonant waveguides generally focus on solutions $n_{\text{eff}} < n_a$, the first solution that is found in this domain is commonly labeled LP_{01}. This leads to the existence of an LP_{01} mode in each transmission window of an ARE. However, from our perspective a more accurate the correct way of labeling LP modes in AREs is starting the search of eigenmodes at the highest refractive index $n_{\text{eff}} = n_g$. This has the consequence that the lowest-order antiresonant mode inside the first transmission window is the LP_{02} mode of the ARE, exhibiting two maxima in its intensity distribution: one in the center of the ARE and the second one inside (or near to) the silica ring.

Figure 2 shows an example of a band map (bands are indicated by the colored areas) calculated from $V = 0.15\pi$ to 1.10π, comprising the LP_{l1} and LP_{l2} resonances (with l being the azimuthal mode order). Qualitatively, one can see two types of modes: (i) such of low-order bands with effective indices exhibiting moderate slopes and (ii) those of a large number of very narrow, highly dispersive bands forming a quasi-continuum of ARE-modes. For the sake of clarity the transparency of all bands has been increased (exponentially) towards higher azimuthal mode orders (i.e., higher numbers of l) to prevent figure cluttering. This representation clearly reveals the advantage of our method compared to rigorous FE simulations since it is possible to target selected mode orders instead of obtaining the entire quasi-continuum of modes, which is the case in full numerical FE simulations. It is interesting to note that the effective indices around the center of the transmission bands can be well approximated by the analytic formula of an isolated glass annulus with large core diameter [28] (black dashed lines in Fig. 2).

As shown in Fig. 2, the effective index of the fundamental core mode of this example fiber geometry (calculated using FE modelling) is located well above the effective index of the fundamental ARE mode since $D_c > d$. A high-resolution FE simulation of the effective index of the fundamental core mode shows that it undergoes a multitude of anti-crossings (not shown here) with the low-azimuthal-mode-order ARE bands towards the low frequency side of each
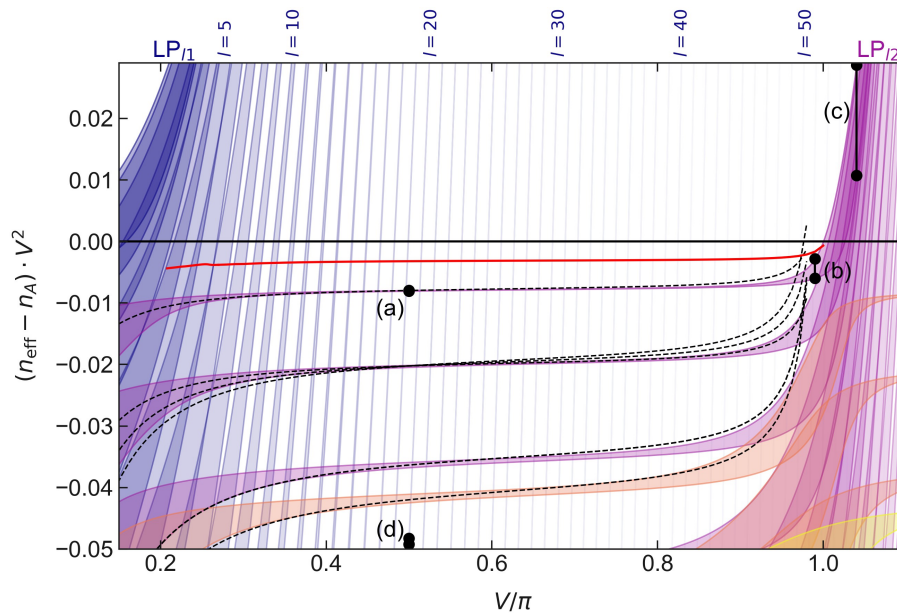
Fig. 2. Band map (colored background) showing the formed ARE-bands between the LP_{l1} and LP_{l2} resonances (parameters given in the main text). Colors refer to different radial mode orders, while selected azimuthal mode orders l are labeled at the top of the graph. The red line refers to the fundamental core mode of the revolver-type HC-ARF obtained from FE-simulations while the black dashed lines correspond to the effective indices of the lowest-order ARE modes calculated using Eq. (25) of [28]. The black markers show the positions of the radial intensity distributions investigated in Fig. 3(a)-(d).

transmission band. This is a result of the decreasing inhibited coupling effect between core and ARE modes in case of low azimuthal mode orders (i.e., small values of l). The emergence of multiple anti-crossings is, in fact, not visible at the high frequency edge (towards higher values of V) of each transmission window. This suggests, that applications which demand a well-behaved group velocity dispersion of the core mode, e.g., applications involving ultrashort pulse propagation, should not operate at the low-frequencies edge (long-wavelength edge) of a transmission window.

Figure 3 shows the normalized intensity distributions of the LP_{02} ARE top and bottom edge mode exemplary for three different V-parameters as well as the intensity distribution of one of the highly disperse bands ($l = 20$, $m = 1$) at $V/\pi = 0.5$. Inside a transmission band, i.e. between two integer multiples of V/π the intensity of the lowest-azimuthal-order ARE modes is dominantly located inside the central air domain of an ARE (see Fig. 3(a)). Since the planar V-parameter corresponds to the accumulated phase between two reflections at the strand [28], the shape of the intensity distribution also correlates with V. As shown in the inset, there is only a negligible amount of light propagating outside the ARE ($r > b$), strongly decreasing the difference of the effective indices of the top and bottom band edge ARE modes, corresponding to a small bandwidth of the LP_{02} band at $V/\pi = 0.50$ (see Fig. 2). Around the resonance frequency, e.g. $V/\pi = 0.99$, the intensity of the ARE modes is distributed more and more inside the air domain outside the annulus ($r > b$). This is accompanied with a larger impact of the different boundary conditions and therefore, results in a significant broadening of the band around the resonances. For frequencies higher than $V/\pi = 1$ the normalized effective indices of the top and bottom band edge LP_{02} mode is positive and therefore, is evanescent in the air domains. A very interesting
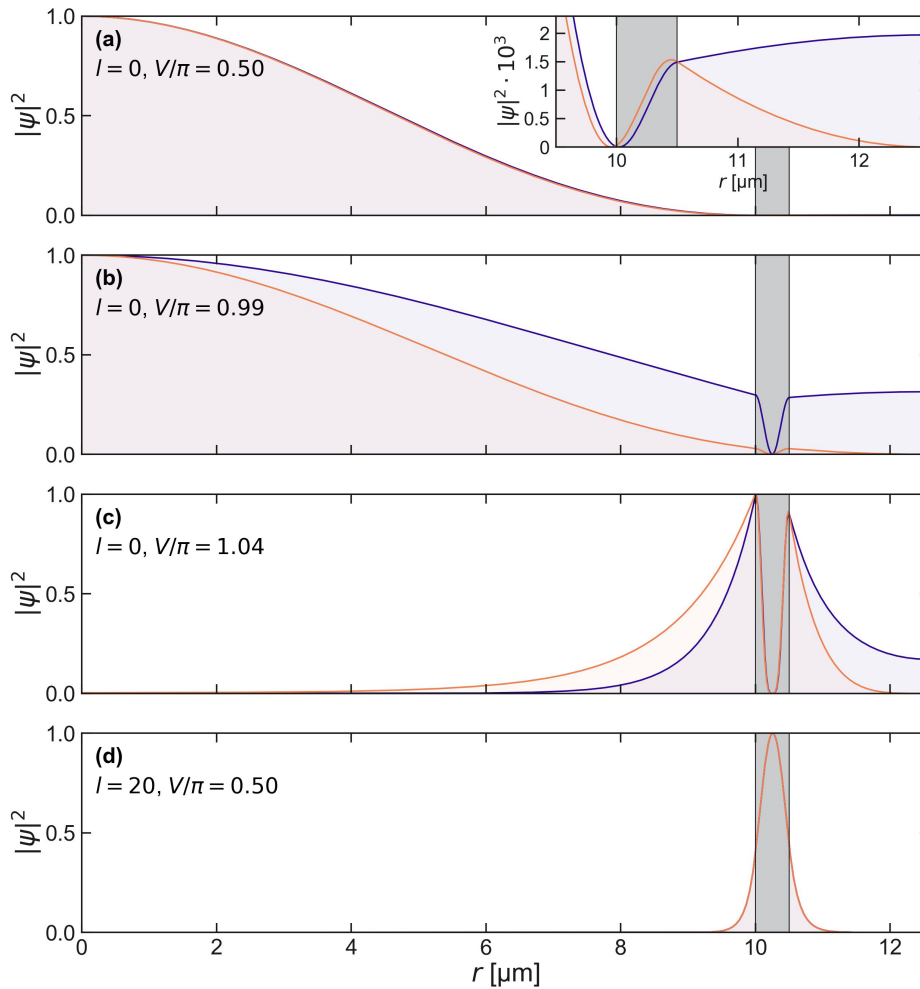
Fig. 3.   Normalized intensity distribution of the top and bottom band edge of the LP_{02} ARE mode (a) in the center of the transmission band ($V = 0.50\pi$), (b) slightly below the first resonance ($V = 0.99\pi$) and (c) after the first resonance ($V = 1.04\pi$). (d) A typical intensity distribution of a higher azimuthal order mode ($l = 20$) at the point of antiresonance ($V = 0.50\pi$). All four plots refer to the positions highlighted by the black dots in Fig. 2.

feature of the AREs can be explained when taking a closer look to the intensity distribution of higher-azimuthal-order modes (see Fig. 3(d)). The intensity is located mainly inside the silica ring, even though the normalized effective index is well below zero. As a consequence, the overlap of the fundamental mode of the whole fiber geometry with such kind of mode is quite small, proving the concept of inhibited coupling in HC-ARFs.

3.3.   Large bandwidth mapping

The simulation of the band map across a significantly larger spectral bandwidth, i.e., a large number of LP_{lm} resonances exhibits similar features as discussed for Fig. 2: well-separated low-order ARE bands that branch-off at the frequencies of the strand resonances (i.e., at V-parameters being a multiple of π) and highly dispersive higher-order ARE bands (Fig. 4). It is important to point out that each radial mode order m supports a larger number of azimuthal mode orders l for

increasing V, overlapping with bands of lower radial mode orders and therefore, increasing the density of ARE modes towards higher frequencies.
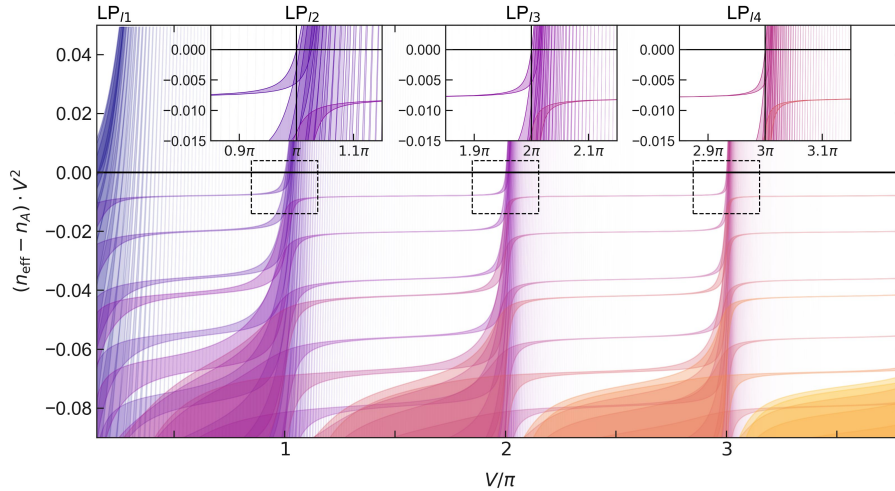

Fig. 4. Band map over a large frequency range calculated using our mathematical model (simulation parameters are given in the main text). Different colors correspond to different radial mode orders m of the LP_{lm} modes. The transparency of the bands scales inversely with the azimuthal mode order l in order to improve visibility and to prevent figure cluttering. The three insets show close-ups of the band map in the vicinity of the resonance points at $V/\pi = 1, 2$ and 3 (highlighted by the black dashed rectangles in the main figure).

3.4. Number of modes of a single ARE

Since the circumference of an ARE is large compared to the operation wavelength, the number of modes supported by a single ARE is high as well, i.e., high azimuthal mode orders have to be considered, leading to very fine-featured density of states maps when using FE-based simulations [27]. In order to save calculation time, we determine the maximum azimuthal mode order that is needed to be taken into account at a certain V-parameter. As shown in the Appendix, the cut-off condition $n_{\text{eff}} = n_a$ for a single ARE leads to the following equation that has to be solved:

$$J_{l+1}(V \cdot a/t)Y_{l-1}(V \cdot b/t) = Y_{l+1}(V \cdot a/t)J_{l-1}(V \cdot b/t). \qquad (2)$$

The number of guided modes M at a certain V-parameter can be obtained by summation of the number of solutions of Eq. (2), considering that the LP_{0m} solution represents two modes and all other solutions represent four modes [52]. Figure 5 shows the results of these calculations as a function of the planar V-parameter for various ratios of d/t. As expected, a large number of modes that increase towards larger V and d/t (hundreds to thousands) are supported by the ARE. Even in the fundamental transmission window ($0 < V \leq \pi$), usually used for light transmission in HC-ARFs, a few hundred modes can be found in an ARE. This particular fact clearly distinguishes HC-ARFs from other low-index core fibers such as all-solid or hollow-core PBG fibers and is a result of the large diameter of the ARE compared to the operation wavelength as well as the comparably high refractive index difference between silica and air. From the perspective of phase-matching, the dispersion of the central core mode undergoes multiple crossing with ARE-modes naively suggesting a coupling of the core mode to leaky ARE modes

at almost any wavelength, making low-loss guidance in HC-ARF not obvious. However, as pointed out by Debord et al. [27], inhibited coupling of the core mode to higher-order modes has to be additionally considered to explain light guidance in HC-ARFs. In their supplementary information it is stated that the overlap integral of the electric fields of the core mode and ARE modes quickly decreases for increasing azimuthal mode orders, qualitatively explaining the emergence of low-loss guidance in HC-ARFs.
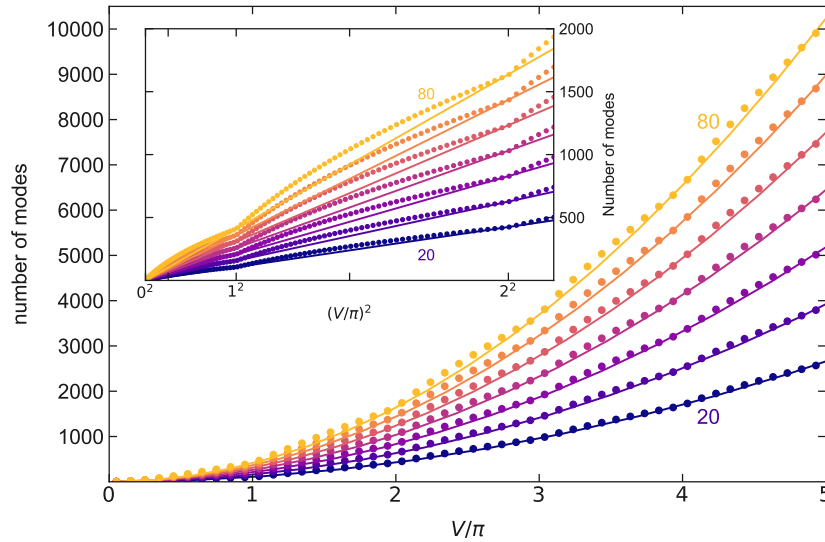

Fig. 5. Number M of ARE-modes as function of the planar waveguide parameter for various d/t ratios ($20 \leq d/t \leq 80$ in increments of 10). The example geometry considered for the band maps is defined by $d/t = 40$. Circles represent the sum of all modes using Eq. (2). Lines correspond to Eq. (3) which is a fit to the data points. The inset shows the number of modes as function of V^2 in order to visualize the quadratic dependence.

The results of Fig. 5 suggests that the number of modes M in an ARE scales linearly with V^2 and d/t, i.e. with the area of the silica domain of an ARE $A = \pi t^2 (1 + d/t) \propto (1 + d/t)V^2$. Fitting such a function to the data points using only a single proportionality parameter yields the following approximation for the number of ARE modes in a silica HC-ARF:

$$M \approx 0.512 \left(1 + \frac{d}{t}\right) \cdot V^2. \tag{3}$$

This equation agrees very well with the simulation results for all considered ratios d/t and V-parameters. Furthermore, it is consistent with the number of modes in multimode fibers (corresponding to the limit $d \to 0$), where $M \approx 0.5V^2$ [52]. The data show discontinuities of the slope at integer values of V/π (see inset of Fig. 5), resulting from the additional set of modes that contribute when sweeping across the resonances of different radial mode order.

3.5. Influence of distance between the AREs

To exemplify that the presented approach allows to solely concentrate on modes that are relevant for the light guidance, we calculate the band maps for three different ARE separation distances ($s = 2\,\mu m$, $5\,\mu m$ and $10\,\mu m$) while keeping the ARE diameter and strand thickness fixed, taking into account exclusively the six lowest azimuthal mode orders only ($0 \leq l \leq 5$, Fig. 6).
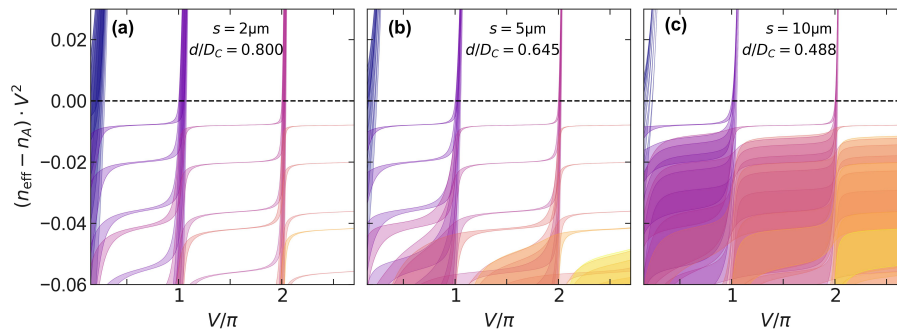
Fig. 6. Dependence of the band maps on the inter-ARE distance s while d and t were kept constant ((a) $s = 2\,\mu m$, (b) $s = 5\,\mu m$, (c) $s = 10\,\mu m$).

Interestingly, small separation distances (large d/D_c) yield band maps with well-separated and comparably narrow bands between the resonance frequencies (Figs. 6(a) and 6(b)), while the bands become substantially wider towards larger ARE separations (smaller d/D_c, Fig. 6(c)). In the latter example already all bands except the lowest-order band in each spectral transmission window overlap. A further increase of ARE distance would result in effective indices of the top bands edges approach levels similar to that of the fundamental core mode of the HC-ARF. The appearance of such wide bands can be explained by the increasing localization of the modes inside the spatial domain between two AREs towards larger separations.

4.   Conclusions

Understanding the modal behavior is of essential importance for any photonic system and is particularly relevant for hollow-core optical fibers that rely on sophisticated light guidance mechanisms. In this work we have presented a semi-analytical model that allows for the determination of the effective indices of the bands formed by the supermodes of the AREs in revolver-type hollow-core fibers. Our approach does not enforce an artificial two-dimensional lattice structure and is particularly useful to understand the behavior of the modes with effective indices smaller than that of air, which is of great importance for understanding light guidance in hollow-core fibers. The model only demands solving two transcendental equations, reducing simulation times by orders of magnitude compared to full numerical simulations and allows to concentrate on modes of pre-chosen order. However, it is noteworthy to mention that the current version of our model is principally limited to symmetric ARE geometries (i.e., structures with azimuthal invariance) while a modified version may be able to handle more complex geometries such as, e.g. nested AREs [53, 54]. We showed that the band maps of revolver-type HC-ARFs consists of (i) low-order ARE-modes with dispersions of moderate slope that branch-off from the isolated LP-resonances and (ii) a larger number of highly dispersive higher-order ARE-modes, forming a quasi-continuum of modes. The latter fact clearly distinguishes HC-ARFs from PBG fibers which have zero density of cladding states in defined spectral domains, therefore highlighting the inhibited coupling effect to be an essential feature of the light guidance in HC-ARFs. By analyzing the modal behavior at cut-off we have shown that the mode density scales by the square of the planar waveguide parameter V, similar to the behavior of multimode fibers. The large amount of modes clearly motivates the application of our model which, in contrast to finite-element simulations, allows to calculate a selected number of modes of prechosen order. We believe that the proposed method represents a very promising tool for future design studies of HC-ARFs, opening new avenues for issues such as modal discrimination via phase-matching of higher-order core modes to continuum modes.

Appendix

Scalar wave equation and dispersion equation

For negative normalized effective indices ($n_{\text{eff}} < n_a$) the radial component of the wave function $\psi(r)$ for can be expressed using Bessel's functions:

$$
\psi(r) = \begin{array}{ll}
A_1 J_l\left(Qr/t\right) & 0 \leq r < a \\
A_2 J_l\left(Ur/t\right) + B_2 Y_l\left(Ur/t\right) & a \leq r \leq b \\
A_3 J_l\left(Qr/t\right) + B_3 Y_l\left(Qr/t\right) & r > b
\end{array}
\tag{4}
$$

where we have normalized U and Q analogous to the V-parameter as

$$
U^2 = k_0^2 t^2 \left(n_g^2 - n_{\text{eff}}^2\right)
\tag{5}
$$

$$
Q^2 = k_0^2 t^2 \left(n_a^2 - n_{\text{eff}}^2\right)
\tag{6}
$$

The continuity of ψ and ψ' at $r = a$ and $r = b$ yields

$$
A_2 = \frac{\pi}{2}\alpha \left[QY_l(U\alpha)J_{l+1}(Q\alpha) - UY_{l+1}(U\alpha)J_l(Q\alpha)\right] A_1
\tag{7}
$$

$$
B_2 = -\frac{\pi}{2}\alpha \left[QJ_l(U\alpha)J_{l+1}(Q\alpha) - UJ_{l+1}(U\alpha)J_l(Q\alpha)\right] A_1
\tag{8}
$$

$$
\begin{aligned}
A_3 = &-\frac{\pi}{2}\beta \left[QJ_l(U\beta)Y_{l+1}(Q\beta) - UJ_{l+1}(U\beta)Y_l(Q\beta)\right] A_2 \\
&-\frac{\pi}{2}\beta \left[QY_l(U\beta)Y_{l+1}(Q\beta) - UY_{l+1}(U\beta)Y_l(Q\beta)\right] B_2
\end{aligned}
\tag{9}
$$

$$
\begin{aligned}
B_3 = &\frac{\pi}{2}\beta \left[QJ_l(U\beta)J_{l+1}(Q\beta) - UJ_{l+1}(U\beta)J_l(Q\beta)\right] A_2 \\
&+\frac{\pi}{2}\beta \left[QY_l(U\beta)J_{l+1}(Q\beta) - UY_{l+1}(U\beta)J_l(Q\beta)\right] B_2
\end{aligned}
\tag{10}
$$

where $\alpha = a/t$ and $\beta = b/t$.

The dispersion equation g_{top} and g_{bot} for the calculation of the effective indices of the top and bottom band edge, respectively, are therefore

$$
g_{\text{top}} = \left\{A_3 \left[J_{l-1}\left(Q\gamma\right) - J_{l+1}\left(Q\gamma\right)\right] + B_3 \left[Y_{l-1}\left(Q\gamma\right) - Y_{l+1}\left(Q\gamma\right)\right]\right\} /Q^{l-1} = 0
\tag{11}
$$

$$
g_{\text{bot}} = \left[A_3 J_l\left(Q\gamma\right) + B_3 Y_l\left(Q\gamma\right)\right] /Q^l = 0
\tag{12}
$$

where we have used $\gamma = c/t$.

Similarly, for values $n_{\text{eff}} > n_a$ the radial part of the wave function $\psi(r)$ can be written as:

$$
\psi(r) = \begin{array}{ll}
A_1 I_l\left(Wr/t\right) & 0 \leq r < a \\
A_2 J_l\left(Ur/t\right) + B_2 Y_l\left(Ur/t\right) & a \leq r \leq b \\
A_3 I_l\left(Wr/t\right) + B_3 K_l\left(Wr/t\right) & r > b
\end{array}
\tag{13}
$$

with $W^2 = k_0^2 t^2 \left(n_{\text{eff}}^2 - n_a^2\right)$, yielding

$$A_2 = -\frac{\pi}{2}\alpha \left[WY_l(U\alpha)I_{l+1}(W\alpha) + UY_{l+1}(U\alpha)I_l(Q\alpha) \right] A_1 \tag{14}$$

$$B_2 = \frac{\pi}{2}\alpha \left[WJ_l(U\alpha)I_{l+1}(W\alpha) + UJ_{l+1}(U\alpha)I_l(W\alpha) \right] A_1 \tag{15}$$

$$\begin{aligned}A_3 = {}& \beta \left[WJ_l(U\beta)K_{l+1}(W\beta) - UJ_{l+1}(U\beta)K_l(W\beta) \right] A_2 \\ & + \beta \left[WY_l(U\beta)K_{l+1}(W\beta) - UY_{l+1}(U\beta)K_l(W\beta) \right] B_2 \end{aligned} \tag{16}$$

$$\begin{aligned}B_3 = {}& \beta \left[WJ_l(U\beta)I_{l+1}(W\beta) + UJ_{l+1}(U\beta)I_l(W\beta) \right] A_2 \\ & + \beta \left[WY_l(U\beta)I_{l+1}(W\beta) + UY_{l+1}(U\beta)I_l(W\beta) \right] B_2 \end{aligned} \tag{17}$$

and therefore, resulting in the following dispersion equations:

$$g_{\text{top}} = A_3 \left\{ \left[I_{l-1}(W\gamma) + I_{l+1}(W\gamma) \right] + B_3 \left[K_{l-1}(W\gamma) + K_{l+1}(W\gamma) \right] \right\} / W^{l-1} = 0 \tag{18}$$

$$g_{\text{bot}} = \left[A_3 J_l(Q\gamma) + B_3 Y_l(Q\gamma) \right] / W^l = 0 \tag{19}$$

Applicability of the scalar approximation

Since our model relies on a scalar description of the electric field (weak-guidance approximaton), it is crucial to ensure that this approximation is justified for refractive-index differences in the magnitude of 0.45 (corresponding to a silica/air interface). Figure 7 shows a direct comparison of the normalized effective index of the lowest-order ARE modes between a vectorial and scalar transfer-matrix approach for the case of a single ARE. One can see that both solutions match very well over a large spectral range inside the first optical window ($1 \le V/\pi \le 2$), in particular for the lowest-order modes. Merely around the resonance points (corresponding to integer values of V/π) the scalar solutions exhibit variations from those of the vectorial wave equation. Therefore, we believe it is reasonable to utilize the scalar wave approximation for the derivation of the presented model in the case of a silica hollow-core fiber.
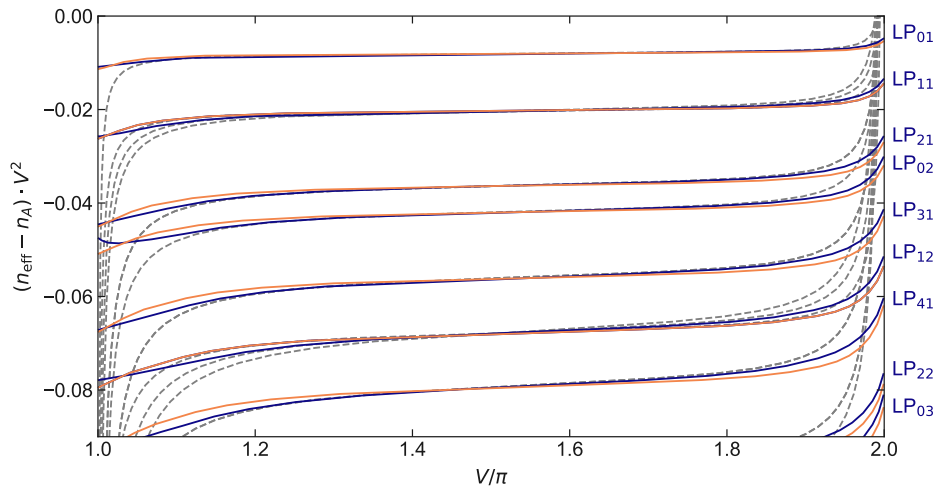

Fig. 7. Comparison between solutions from the vectorial (solid blue lines) and scalar (solid orange lines) wave equation for a single ARE. The dashed grey curves correspond to the solutions of Eq. (25) from [28].

Funding

References

1. R. Sollapur, D. Kartashov, M. Zürch, A. Hoffmann, T. Grigorova, G. Sauer, A. Hartung, A. Schwuchow, J. Bierlich, J. Kobelke, M. Chemnitz, M. A. Schmidt, and C. Spielmann, "Resonance-enhanced multi-octave supercontinuum generation in antiresonant hollow-core fibers," Light Sci. Appl. **6**(12), e17124 (2017).
2. P. S. J. Russell, P. Hölzer, W. Chang, A. Abdolvand, and J. C. Travers, "Hollow-core photonic crystal fibres for gas-based nonlinear optics," Nat. Photon. **8**(4), 278–286 (2014).
3. A. Hartung, J. Kobelke, A. Schwuchow, J. Bierlich, J. Popp, M. A. Schmidt, and T. Frosch, "Low-loss single-mode guidance in large-core antiresonant hollow-core fibers," Opt. Lett. **40**(14), 3432–3435 (2015).
4. S. Fei Gao, Y. Ying Wang, W. Ding, D. Liang Jiang, S. Gu, X. Zhang, and P. Wang, "Hollow-core conjoined-tube negative-curvature fibre with ultralow loss," Nat. Commun. **9**(1), 2828 (2018).
5. F. Yu, M. Cann, A. Brunton, W. Wadsworth, and J. Knight, "Single-mode solarization-free hollow-core fiber for ultraviolet pulse delivery," Opt. Express **26**(8), 10879–10887 (2018).
6. F. Yu, W. J. Wadsworth, and J. C. Knight, "Low loss silica hollow core fibers for 3-4 μm spectral region," Opt. Express **20**(10), 11153–11158 (2012).
7. A. N. Kolyadin, A. F. Kosolapov, A. D. Pryamikov, A. S. Biriukov, V. G. Plotnichenko, and E. M. Dianov, "Light transmission in negative curvature hollow core fiber in extremely high material loss region," Opt. Express **21**(8), 9514–9519 (2013).
8. M. Xu, F. Yu, and J. Knight, "Mid-infrared 1W hollow-core fiber gas laser source," Opt. Lett. **42**(20), 4055–4058 (2017).
9. L. Cao, S.-F. Gao, Z.-G. Peng, X.-C. Wang, Y.-Y. Wang, and P. Wang, "High peak power 28 μm Raman laser in a methane-filled negative-curvature fiber," Opt. Express **26**(5), 5609–5615 (2018).
10. M. Xu, F. Yu, M. R. Hassan, and J. C. Knight, "Continuous-wave mid-infrared gas fiber lasers," IEEE J. Sel. Top. Quantum Electron. **24**(3), 1-8 (2018).
11. M. I. Hasan, N. Akhmediev, and W. Chang, "Empirical formulae for dispersion and effective mode area in hollow-core antiresonant fibers," J. Light. Technol. **36**(18), 4060–4065 (2018).
12. S. O. Konorov, C. J. Addison, H. G. Schulze, R. F. B. Turner, and M. W. Blades, "Hollow-core photonic crystal fiber-optic probes for Raman spectroscopy," Opt. Lett. **31**(12), 1911–1913 (2006).
13. P. Ghenuche, S. Rammler, N. Y. Joly, M. Scharrer, M. Frosz, J. Wenger, P. S. J. Russell, and H. Rigneault, "Kagome hollow-core photonic crystal fiber probe for Raman spectroscopy," Opt. Lett. **37**(21), 4371–4373 (2012).
14. M. A. Popenda, N. H. Stawska, L. M. Mazur, K. Jakubowski, A. Kosolapov, A. Kolyadin, and E. Bereś-Pawlik, "Application of negative curvature hollow-core fiber in an optical fiber sensor setup for multiphoton spectroscopy," Sensors **17**(10), 2278 (2017).
15. W. Jin, Y. Cao, F. Yang, and H. L. Ho, "Ultra-sensitive all-fibre photothermal spectroscopy with large dynamic range," Nat. Commun. **6**, 6767 (2015).
16. M. Nissen, B. Doherty, J. Hamperl, J. Kobelke, K. Weber, T. Henkel, and M. A. Schmidt, "UV absorption spectroscopy in water-filled antiresonant hollow core fibers for pharmaceutical detection," Sensors **18**(2), 478 (2018).
17. V. Sandfort, B. M. Trabold, A. Abdolvand, C. Bolwien, P. S. J. Russell, J. Wöllenstein, and S. Palzer, "Monitoring the wobbe index of natural gas using fiber-enhanced Raman spectroscopy," Sensors **17**(12), 2714 (2017).
18. P. Jaworski, F. Yu, R. R. Maier, W. J. Wadsworth, J. C. Knight, J. D. Shephard, and D. P. Hand, "Picosecond and nanosecond pulse delivery through a hollow-core Negative Curvature Fiber for micro-machining applications," Opt. Express **21**(19), 22742–22753 (2013).
19. B. Debord, M. Alharbi, L. Vincetti, A. Husakou, C. Fourcade-Dutin, C. Hoenninger, E. Mottay, F. Gérôme, and F. Benabid, "Multi-meter fiber-delivery and pulse self-compression of milli-Joule femtosecond laser and fiber-aided laser-micromachining," Opt. Express **22**(9), 10735–10746 (2014).
20. A. Urich, R. R. J. Maier, F. Yu, J. C. Knight, D. P. Hand, and J. D. Shephard, "Flexible delivery of Er:YAG radiation at 294 μm with negative curvature silica glass fibers: a new solution for minimally invasive surgical procedures," Biomed. Opt. Express **4**(2), 193–205 (2013).
21. M. Banu, S. Nawazuddin, N. V. Wheeler, J. R. Hayes, S. R. Sandoghchi, T. D. Bradley, G. T. Jasion, and R. Slav, "Lotus-shaped negative curvature hollow core fiber with 10.5 dB/km at 1550 nm wavelength," J. Light. Technol. **36**(5), 1213–1219 (2018).
22. J. R. Hayes, S. R. Sandoghchi, T. D. Bradley, Z. Liu, R. Slavik, M. A. Gouveia, N. V. Wheeler, G. Jasion, Y. Chen, E. N. Fokoua, M. N. Petrovich, D. J. Richardson, and F. Poletti, "Antiresonant hollow core fiber with an octave spanning bandwidth for short haul data communications," J. Light. Technol. **35**(3), 437–442 (2017).
23. F. Gérôme, R. Jamier, J.-L. Auguste, G. Humbert, and J.-M. Blondy, "Simplified hollow-core photonic crystal fiber," Opt. Lett. **35**(8), 1157–1159 (2010).
24. A. D. Pryamikov, A. S. Biriukov, A. F. Kosolapov, V. G. Plotnichenko, S. L. Semjonov, and E. M. Dianov, "Demonstration of a waveguide regime for a silica hollow - core microstructured optical fiber with a negative curvature of the core boundary in the spectral region >3.5 μm," Opt. Express **19**(2), 1441–1448 (2011).

25. M. A. Duguay, Y. Kokubun, T. L. Koch, and L. Pfeiffer, "Antiresonant reflecting optical waveguides in SiO_2-Si multilayer structures," Appl. Phys. Lett. **49**(1), 13–15 (1986).
26. N. M. Litchinitser, A. K. Abeeluck, C. Headley, and B. J. Eggleton, "Antiresonant reflecting photonic crystal optical waveguides," Opt. Lett. **27**(18), 1592–1594 (2002).
27. B. Debord, A. Amsanpally, M. Chafer, A. Baz, M. Maurel, J. M. Blondy, E. Hugonnot, F. Scol, L. Vincetti, F. Gérôme, and F. Benabid, "Ultralow transmission loss in inhibited-coupling guiding hollow fibers," Optica **4**(2), 209–217 (2017).
28. M. Zeisberger and M. A. Schmidt, "Analytic model for the complex effective index of the leaky modes of tube-type anti-resonant hollow core fibers," Sci. Rep. **7**(1), 11761 (2017).
29. M. Bache, M. S. Habib, C. Markos, and J. Lægsgaard, "Poor-man's model of hollow-core anti-resonant fibers," J. Opt. Soc. Am. B **36**(1), 69–80(2018).
30. W. Belardi and J. C. Knight, "Hollow antiresonant fibers with low bending loss," Opt. Express **22**(8), 10091–10096 (2014).
31. Y. Y. Wang, N. V. Wheeler, F. Couny, P. J. Roberts, and F. Benabid, "Low loss broadband transmission in hypocycloid-core Kagome hollow-core photonic crystal fiber," Opt. Lett. **36**(5), 669–671 (2011).
32. W. Belardi and J. C. Knight, "Effect of core boundary curvature on the confinement losses of hollow antiresonant fibers," Opt. Express **21**(19), 21912–21917 (2013).
33. W. Belardi and J. C. Knight, "Hollow antiresonant fibers with reduced attenuation," Opt. Lett. **39(7)**, 1853–1856 (2014).
34. F. Poletti, "Nested antiresonant nodeless hollow core fiber," Opt. Express **22**(20), 23807–23828 (2014).
35. W. Belardi, "Design and properties of hollow antiresonant fibers for the visible and near infrared spectral range," J. Light. Technol. **33**(21), 4497–4503 (2015).
36. D. Bird, "Attenuation of model hollow-core, anti-resonant fibres," Opt. Express **25**(19), 23215–23237 (2017).
37. F. Couny, F. Benabid, P. J. Roberts, P. S. Light, and M. G. Raymer, "Generation and photonic guidance of multi-octave optical-frequency combs," Science **318**(5853), 1118–1121 (2007).
38. A. M. Zheltikov, "Ray-optic analysis of the (bio)sensing ability of ring-cladding hollow waveguides," Appl. Opt. **47**(3), 474–479 (2008).
39. W. Ding and Y. Wang, "Analytic model for light guidance in single-wall hollow-core anti-resonant fibers," Opt. Express **22**(22), 27242–27256 (2014).
40. Y. Wang and W. Ding, "Confinement loss in hollow-core negative curvature fiber: A multi-layered model," Opt. Express **25**(26), 33122–33133 (2017).
41. M. H. Frosz, P. Roth, M. C. Günendi, and P. S. Russell, "Analytical formulation for the bend loss in single-ring hollow-core photonic crystal fibers," Photonics Res. **5**(2), 88–91 (2017).
42. F. Luan, A. K. George, T. D. Hedley, G. J. Pearce, D. M. Bird, J. C. Knight, and P. S. J. Russell, "All-solid photonic bandgap fiber," Opt. Lett. **29**(20), 2369–2371 (2004).
43. S. John, "Strong localization of photons in certain disordered dielectric superlattices," Phys. Rev. Lett. **58**(23), 2486–2489 (1987).
44. E. Yablonovitch, T. Gmitter, and K. Leung, "Photonic band structure: The face-centered-cubic case employing nonspherical atoms," Phys. Rev. Lett. **67**(17), 2295–2298 (1991).
45. J. Pottage, D. Bird, T. Hedley, J. Knight, T. Birks, P. Russell, and P. Roberts, "Robust photonic band gaps for hollow core guidance in PCF made from high index glass," Opt. Express **11**(22), 2854–2861 (2003).
46. T. A. Birks, G. J. Pearce, and D. M. Bird, "Approximate band structure calculation for photonic bandgap fibres," Opt. Express **14**(20), 9483–9490 (2006).
47. T. Grujic, B. T. Kuhlmey, C. M. de Sterke, and C. G. Poulton, "Modelling of photonic crystal fiber based on layered inclusions," J. Opt. Soc. Am. B **26**(10), 1852–1861 (2009).
48. N. Granzow, P. Uebel, M. A. Schmidt, A. S. Tverjanovich, L. Wondraczek, and P. S. J. Russell, "Bandgap guidance in hybrid chalcogenide-silica photonic crystal fibers," Opt. Lett. **36**(13), 2432–2434 (2011).
49. R. Spittel, H. Bartelt, and M. A. Schmidt, "A semi-analytical model for the approximation of plasmonic bands in arrays of metal wires in photonic crystal fibers," Opt. Express **22**(10), 11741–11753 (2014).
50. P. Uebel, M. C. Günendi, M. H. Frosz, G. Ahmed, N. N. Edavalath, J.-M. Ménard, and P. S. Russell, "Broadband robustly single-mode hollow-core PCF by resonant filtering of higher-order modes," Opt. Lett. **41**(9), 1961–1964 (2016).
51. E. A. Marcatili and R. A. Schmeltzer, "Hollow metallic and dielectric waveguides for long distance optical transmission and lasers," Bell Syst. Tech. J. **43**(4), 1783–1809 (1964).
52. D. Gloge, "Weakly guiding fibers," Appl. Opt. **10**(10), 2252–2258 (1971).
53. M. I. Hasan, N. Akhmediev, and W. Chang, "Positive and negative curvatures nested in an antiresonant hollow-core fiber," Opt. Lett. **42**(4), 703–706 (2017).
54. M. S. Habib, J. E. Antonio-Lopez, C. Markos, A. Schülzgen, and R. Amezcua-Correa, "Single-mode, low loss hollow-core anti-resonant fiber designs," Opt. Express **27**(4), 3824–3836 (2019).